Available online at www.sciencedirect.com

ScienceDirect

Geochimica et Cosmochimica Acta 315 (2021) 73–88

Geochimica et Cosmochimica Acta

www.elsevier.com/locate/gca

Dating martian mafic crust; microstructurally constrained baddeleyite geochronology of enriched shergottites Northwest Africa (NWA) 7257, NWA 8679 and Zagami

Leanne G. Staddon [a,*], James R. Darling [a], Winfried H. Schwarz [b], Natasha R. Stephen [c], Sheila Schuindt [a], Joseph Dunlop [a], Kimberly T. Tait [d]

[a] *School of the Environment, Geography and Geoscience, University of Portsmouth, Portsmouth PO1 3QL, United Kingdom*
[b] *Institute of Earth Sciences, Heidelberg Ion Probe, Heidelberg University, 69120 Heidelberg, Germany*
[c] *Plymouth Electron Microscopy Centre, University of Plymouth, Plymouth PL4 8AA, United Kingdom*
[d] *Department of Natural History, Royal Ontario Museum, Toronto, ON M5S 2C6, Canada*

Received 21 April 2021; accepted in revised form 27 September 2021; Available online 5 October 2021

Abstract

Baddeleyite (monoclinic; *m*-ZrO_2) is a widespread accessory phase within shergottites. However, the effects of shock loading on baddeleyite U-Pb isotopic systematics, and therefore its reliability as a geochronometer within highly shocked lithologies, are less well constrained. To investigate the effects of shock metamorphism on baddeleyite U-Pb chronology, we have conducted high-resolution microstructural analysis and *in-situ* U-Pb isotopic measurements for baddeleyite within enriched basaltic shergottites Northwest Africa (NWA) 7257, NWA 8679 and Zagami. Electron backscatter diffraction (EBSD) analyses of baddeleyite reveal significant microstructural heterogeneity within individual thin sections, recording widespread partial to complete reversion from high-pressure (≥3.3 GPa) orthorhombic zirconia polymorphs. We define a continuum of baddeleyite microstructures into four groupings on the basis of microstructural characteristics, including rare grains that retain magmatic twin relationships. Uncorrected U-Pb isotopic measurements form Tera-Wasserburg discordia, yielding new ^{238}U-^{206}Pb discordia ages of 195 ± 15 Ma ($n = 17$) for NWA 7257 and 220 ± 23 Ma ($n = 10$) for NWA 8679. Critically, there is no resolvable link between baddeleyite microstructure and U-Pb isotope systematics, indicating negligible open-system behaviour of U-Pb during zirconia phase transformations. Instead, we confirm that high post-shock temperatures exert the greatest control on Pb mobility within shocked baddeleyite; in the absence of high post-shock temperatures, baddeleyite yield robust U-Pb isotope systematics and date the age of magmatic crystallization. Low bulk post-shock temperatures recorded within Zagami (≤220 °C), and suggested within NWA 7257 and NWA 8679 by baddeleyite microstructure and other petrological constraints, confirm that the previously derived baddeleyite age of Zagami records magmatic crystallization, and provide greater age diversity to 225 Ma to 160 Ma enriched shergottites. While our data yield no resolvable link between microstructure and U-Pb isotopic composition, we strongly recommend that microstructural analyses should represent an essential step of baddeleyite U-Pb chronology within planetary (*e.g.,* martian, lunar, asteroidal) and shocked terrestrial samples, allowing full contextualisation prior to destructive isotopic techniques. Microstructurally constrained *in-situ* U-Pb

* Corresponding author.
E-mail address: leanne.staddon@port.ac.uk (L.G. Staddon).

https://doi.org/10.1016/j.gca.2021.09.034

analyses of baddeleyite thus define new opportunities for the absolute chronology of martian meteorites and, more broadly, shocked planetary materials.

Keywords: Baddeleyite; Shergottite; Chronology; EBSD; Shock metamorphism

1. INTRODUCTION

Our ability to place absolute constraints on the timing of martian crustal processes is critical to our understanding of the evolution of the planet's surface and interior. Currently, radiometric dating of martian meteorites is the only direct means to achieve this. The martian meteorite collection is dominated in number and mass by shergottites; ultramafic to mafic rocks grouped according to their petrography, trace element characteristics, and the isotopic composition of their mantle sources (Udry et al., 2020). While crater chronology indicates the martian surface is dominated by ancient, pre-Amazonian crust (*i.e.,* 4.5–3.0 Ga; Hartmann and Berman, 2000), Rb-Sr, Sm-Nd, Lu-Hf and U-Pb isochrons of shergottites dominantly yield late Amazonian ages of $\leq$600 Ma (Nyquist et al., 2001; Udry et al., 2020; Váci and Agee, 2020). This apparent dichotomy led to the shergottite age paradox (Nyquist et al., 2001; Head et al., 2002; Bouvier et al., 2005, 2008, 2009; El Goresy et al., 2013; Moser et al., 2013; Zhou et al., 2013; Bellucci et al., 2016; Darling et al., 2016), with debate strongly centred on the true crystallization age of shergottites and, due to the $\geq$20 GPa shock pressures typically experienced by shergottites during ejection from the martian surface (Fritz et al., 2005), the role of shock resetting in calculated ages (Bouvier et al., 2008; Gaffney et al., 2011; El Goresy et al., 2013; Váci and Agee, 2020).

In-situ U-Pb dating of baddeleyite (monoclinic zirconia; *m*-ZrO_2), a widespread accessory phase within enriched shergottites (Herd et al., 2017), has been key in resolving this conundrum (Moser et al., 2013; Zhou et al., 2013; Darling et al., 2016). Such *in-situ* approaches allow characterization of petrographic context prior to isotopic analyses and are considered less sensitive to perturbation than traditional dating techniques, where preferential leaching, terrestrial or martian contamination, and the inclusion of trace phases may modify the isotopic compositions of mineral separates. Thus far, five U-Pb baddeleyite ages have attested to the late Amazonian age of shergottites: 235 $\pm$ 37 Ma for Roberts Massif (RBT) 04261 (Niihara, 2011), 192 $\pm$ 10 Ma for Grove Mountains (GRV) 020090 (Jiang and Hsu, 2012), 185 $\pm$ 9 Ma for Zagami (Zhou et al., 2013), 187 $\pm$ 33 Ma for Northwest Africa (NWA) 5298 (Moser et al., 2013), and 188 $\pm$ 8 Ma for NWA 8653 (Wu et al., 2021).

Despite the importance of baddeleyite as the dominant U-Pb chronometer within mafic to ultramafic shergottites (Herd et al., 2017), significant uncertainties remain regarding the resilience of baddeleyite U-Pb isotopic compositions during shock metamorphism. There is currently a contradiction between experimental studies of baddeleyite, which retain closed system U-Pb isotope systematics up to shock pressures of ~57 GPa (Niihara et al., 2012), and reported U-Pb isotopic disturbance within natural baddeleyite. This includes up to 80% Pb-loss within baddeleyite from the highly-shocked basaltic shergottite NWA 5298 (bulk shock pressures $\geq$42 GPa; Darling et al., 2016) and age resetting within terrestrial baddeleyite that have experienced 15–20 GPa shock pressures (White et al., 2017). The magnitude of U-Pb isotopic disturbance in baddeleyite from NWA 5298 is closely linked with baddeleyite microstructure (Darling et al., 2016), as determined by electron backscatter diffraction (EBSD). Pb loss is shown to be most pronounced in grains with evidence for recrystallization and transformation to meta-stable, high-pressure (orthorhombic) and/or high-temperature (tetragonal) zirconia polymorphs. Nevertheless, areas of high shock impedance (*e.g.,* resistance to shock wave propagation) within NWA 5298 facilitate the retention of baddeleyite with igneous microstructural characteristics, allowing for the unambiguous resolution of magmatic and impact ages (Darling et al., 2016).

Despite this, microstructurally constrained baddeleyite geochronology has not yet been undertaken in any other shergottite. Furthermore, NWA 5298 experienced elevated bulk shock pressures and post-shock temperatures in comparison to most shergottites (Hui et al., 2011); the magnitude of isotopic disturbance caused by reversion from high P-T zirconia polymorphs within more moderately shocked shergottites, and thus the absolute significance of previous U-Pb isotopic ages, remains unclear. Raman spectra indicative of *m*-ZrO_2 have been used to argue for an absence of high P-T zirconia polymorphs within martian and lunar lithologies (Niihara, 2011; Niihara et al., 2012; Zhou et al., 2013; Wu and Hsu, 2020; Wu et al., 2021). However, zirconia polymorphs are known to be metastable (Cayron et al., 2010), with subsequent reversion resulting in the nucleation of *m*-ZrO_2 domains indistinguishable from magmatic baddeleyite using Raman spectroscopy. This technique therefore cannot be used to conclude an unmodified magmatic origin for baddeleyite within planetary materials, and highlights the necessity of coupled microstructural and chronological analyses of baddeleyite within shocked lithologies.

Here, we conduct high-spatial resolution microstructural analysis and *in-situ* U-Pb geochronology of baddeleyite within three enriched, moderately-shocked basaltic shergottites. We revisit baddeleyite U-Pb isotope systematics within Zagami and produce two new, microstructurally-constrained ages for NWA 7257 and NWA 8679. Our data illustrate the advantages of careful documentation of baddeleyite microstructure prior to isotopic analysis, and highlight the utility of baddeleyite as a geochronometer at shock conditions typically experienced by shergottites and other planetary materials.

1.1. The microstructural response of baddeleyite to shock metamorphism

Baddeleyite is sensitive to shock metamorphism and undergoes a series of transformations to metastable polymorphs with increasing P-T conditions (Fig. 1; Cayron et al., 2010; Timms et al., 2017a,b; White et al., 2018; Takagi et al., 2020). At pressures and temperatures below 3.3 GPa and ca. 1170 °C, respectively, baddeleyite (*m*-ZrO_2) is stable and typically forms simple or polysynthetic {100}, {110} or {001} twins (Smith and Newkirk, 1965). With increasing pressure (≥3.3 GPa; Takagi et al., 2020), *m*-ZrO_2 experiences a series of phase transformations to a series of orthorhombic (*o*-ZrO_2) structures. At temperatures of >1170 °C and >2370 °C, *m*-ZrO_2 undergoes martensitic phase transformation to tetragonal (*t*-ZrO_2) or cubic (*c*-ZrO_2) structures. Polymorphs are unstable at ambient conditions and thus rapidly revert to *m*-ZrO_2, forming domains linked by systematic orientation relationships (ORs) due to the correspondence between daughter *m*-ZrO_2 and the crystallographic symmetry of the parental polymorph (Kelly and Rose, 2002; Cayron et al., 2010; Timms et al., 2017a,b; White et al., 2018). Reversion from *t*-ZrO_2 and *o*-ZrO_2 polymorphs results in the nucleation of orthogonally-related (at 90°) *m*-ZrO_2 domains with irregular morphologies (Cayron et al., 2010; Timms et al., 2017b; White et al., 2018); on pole figures, this is shown as three, orthogonally orientated clusters of *m*-ZrO_2 (Fig. 1b). Microstructural analyses therefore do not currently allow distinction between reversion from *t*-ZrO_2 and *o*-ZrO_2 polymorphs, but may be used in combination with independent constraints on the P-T conditions experienced during shock metamorphism (White et al., 2018). However, it is possible to resolve the presence or absence of baddeleyite phase transformation histories from EBSD analysis for grains that have experienced P-T conditions spanning the full-range of conditions recorded within planetary materials (Darling et al., 2016; White et al., 2017, 2018).

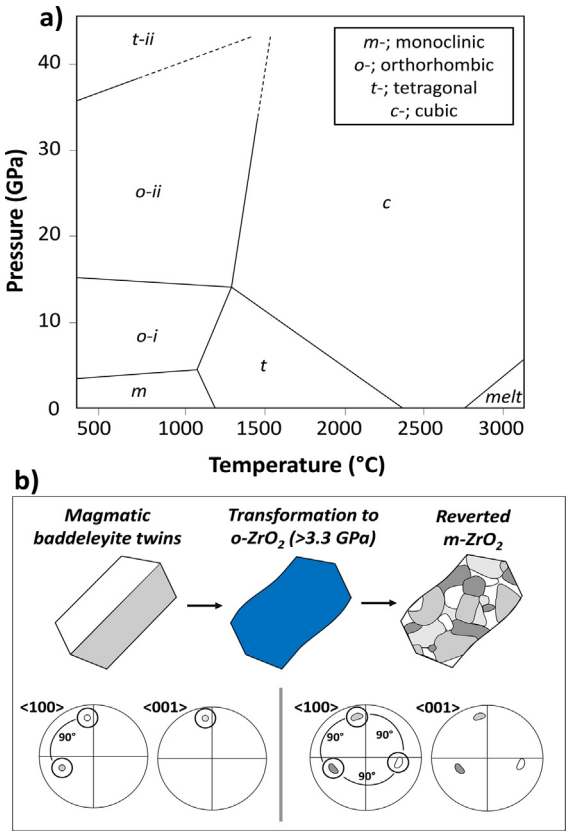

Fig. 1. **(a)** Phase diagram of ZrO_2; *m*; monoclinic, *t*; tetragonal, *o*; orthorhombic, *c*; cubic. Modified after Ohtaka et al. (2001) and Takagi et al. (2020). **(b)** Baddeleyite microstructure upon transformation to and reversion from meta-stable, high-pressure *o*-ZrO_2, which is anticipated given the low post-shock temperatures suggested by bulk shock characteristics (<220 °C; Malavergne et al., 2001; Fritz et al., 2005; Stöffler et al., 2018). Representative orientation relationships (ORs) shown by pole figures. Simple, magmatic twins show a 180° rotation in ⟨001⟩, with a single 90° rotation in ⟨100⟩ and ⟨010⟩ (180°/⟨001⟩ twins). Reversion from orthorhombic precursors results in the nucleation of irregular *m*-ZrO_2 domains that are microstructurally controlled by the symmetry of the parental phase (*e.g.,* all angles 90°, a ≠ b ≠ c); reversion from *o*-ZrO_2 thus results in three clusters of orthogonally related *m*-ZrO_2 in pole figures.

2. MATERIALS AND METHODS

2.1. Studied shergottites

2.1.1. Sample petrography

Northwest Africa 7257, NWA 8679 and Zagami are enriched shergottites (McCoy et al., 1999; Irving et al., 2012; Tait et al., 2015), within which baddeleyite is a widespread accessory phase (Supplementary Fig. A.1). NWA 7257 is a medium-grained shergottite with an intersertal texture (Irving et al., 2012). It is composed predominantly of complexly zoned clinopyroxene, with domains of pigeonite ($Fs_{29.8\text{-}34.3}En_{54.0\text{-}52.4}Wo_{15.3\text{-}13.3}$) and subcalcic augite ($Fs_{21.1\text{-}38.9}En_{46.4\text{-}32.0}Wo_{32.4\text{-}29.1}$), zoning to ferropigeonite rims ($Fs_{44.6\text{-}54.1}En_{44.0\text{-}27.9}Wo_{11.4\text{-}18.0}$), and maskelynite ($An_{44.0\text{-}45.1}Ab_{53.8\text{-}52.2}Or_{2.2\text{-}2.7}$). Accessory phases include ilmenite, ulvöspinel, Fe-sulphide (pyrrhotite), merrillite, Cl-apatite, fayalite, and areas of Si- and K-rich mesostasis (Irving et al., 2012).

NWA 8679 is a basaltic shergottite with an intersertal texture (Tait et al., 2015). It is dominantly composed of patchily zoned clinopyroxene, consisting of subcalcic augite ($Fs_{21.2\text{-}37.2}En_{47.2\text{-}28.9}Wo_{31.6\text{-}33.9}$) and pigeonite ($Fs_{29.9\text{-}59.7}En_{60.3\text{-}23.4}Wo_{9.8\text{-}16.9}$), and maskelynite ($An_{47.9\text{-}54.1}Ab_{50.6\text{-}44.6}Or_{1.5\text{-}1.3}$). Minor phases include ilmenite, ulvöspinel, Fe-sulphide (pyrrhotite), merrillite, Cl-apatite, and areas of Si- and K- rich mesostasis. Mesostasis typically contains super-fine (≤2 μm), acicular baddeleyite.

Finally, Zagami is a basaltic shergottite composed dominantly of 'normal Zagami' (NZ; 80%), an intergranular lithology dominated by pigeonite ($Fs_{28.7\text{-}54.3}En_{55.9\text{-}36.0}Wo_{15.4\text{-}9.7}$), augite ($Fs_{19.5\text{-}35.0}En_{46.1\text{-}32.3}Wo_{34.4\text{-}32.7}$), and maskelynite ($Ab_{43\text{-}53}Ab_{56\text{-}43}Or_{1\text{-}4}$) (McCoy et al., 1999). Dark mottled lithology (DML) represents 20% of Zagami,

and is composed of mm- to cm- scale late stage melt pockets enriched in olivine, silica, phosphates, Fe-Ti oxides and sulphides (McCoy et al., 1999). A volumetrically minor third lithology, named David New (DN), is dominated by olivine and symplectite-rich domains in late stage melt pockets within DML (Vistisen et al., 1992; McCoy et al., 1999).

2.1.2. Shock metamorphism

Evidence of shock metamorphism within the studied samples includes pervasive fracturing of silicates, oxides and phosphates, mosaicism of clinopyroxene, and complete transformation of plagioclase to diaplectic glass (maskelynite). Localised pockets of glassy or partly crystalline shock melt are present in all samples. Within Zagami and NWA 8679, thin veinlets ($\leq$100 μm in width) of shock melt cross cut the entire studied section; thicker veins of shock melt are reported within Zagami elsewhere (McCoy et al., 1992; Fritz et al., 2005). All studied samples yield features indicative of bulk shock pressures in excess of 28 GPa and comparable shock features to the bulk of shergottites (Stöffler et al., 2018). The exact P-T conditions experienced by NWA 7257 and NWA 8679 are unknown, but well studied within Zagami. While shock deformation is an inherently heterogeneous process (Sharp and DeCarli, 2006), most authors state bulk shock pressures for Zagami of ca. 30 GPa (Stöffler et al., 1986; Langenhorst, 2000; Fritz et al., 2005; *cf.* El Goresy et al., 2013). Calculated post-shock temperatures are variable, but low, ranging from ~70 °C to ~220 °C (Stöffler et al., 1986; Nyquist et al., 2001; Fritz et al., 2005). Low bulk post-shock temperatures are in good agreement with nascent shock melt veining and absence of indicators of elevated temperatures, including incipient recrystallization and flow structures within melted plagioclase glass (Stöffler et al., 2018).

2.1.3. Previous geochronological investigations

Cosmic ray exposure (CRE) ages of Zagami and NWA 7257 are 2.8 Ma (Herzog and Caffee, 2014; Wieler et al., 2016), indicating their derivation from Mars within the same ejection event. The ejection age of NWA 8679 is unknown, and no constraints on the crystallization age of NWA 7257 or NWA 8679 have previously been reported. In contrast, the radiometric age of Zagami has been intensively investigated. ^{87}Rb-^{87}Sr and ^{147}Sm-^{143}Nd ages of ca. 180 Ma (*e.g.* Shih et al., 1982) agree with a ^{238}U-^{206}Pb age of 182.7 ± 6.9 Ma (2σ) determined by *in-situ* isotopic analysis of baddeleyite by Zhou et al. (2013). However, baddeleyite analyses lack microstructural characterization, and thus the potential effects of shock metamorphism on the U-Pb systematics have not been evaluated. Slightly younger Rb-Sr and Sm-Nd ages approaching ~160 Ma were also reported by Borg et al. (2005); these isochrons are complex, with leachates yielding disturbed isotopic compositions. An older Ar-Ar age of ~223 Ma is interpreted to represent inherited radiogenic ^{40}Ar (Bogard and Park, 2008). In light of the span of ages reported for Zagami and uncertainties of the geological significance of previous baddeleyite U-Pb ages, the crystallization age of Zagami warrants further investigation.

2.2. Methods

2.2.1. Micro- and nano-structural baddeleyite analysis

Electron microbeam techniques were undertaken using a Zeiss EVO MA10 LaB_6 scanning electron microscope (SEM) at the University of Portsmouth. Thin sections and epoxy mounts were mapped in back scattered electron (BSE) and energy dispersive X-ray spectroscopy (EDS), and baddeleyite grains were identified using Oxford Instruments AZtec Feature software. Analyses were run at an accelerating voltage of 20 kV and a beam current of 1 nA, enabling baddeleyite $\geq$1 μm to be identified. Further vibratory polishing using a 50 nm alumina suspension was undertaken prior to EBSD analyses. EBSD analyses were undertaken using an Oxford Instruments Nordlys-nano detector on the same SEM system. EBSD methods followed those of Darling et al., (2016), using the parameters detailed in Table 1. Data were processed offline using Oxford Instruments Channel 5, where a 'wildspike' correction and noise reduction (level 8) were applied; the first replaces isolated indexed pixels with zero solutions, while the second infills zero solutions when surrounded by at least 8 indexed pixels. Systematic indexing, produced by mirror symmetry of the b-axis in monoclinic systems, has been removed from maps and pole figures; this process is discussed in detail within Supplementary Material A. Microstructural data were principally interpreted using a combination of band contrast (BC), Euler maps, and stereographic projections. BC describes the intensity of Kikuchi bands in relation to the overall electron backscatter pattern (EBSP), highlighting the magnitude of baddeleyite diffraction and crystallinity. Euler maps are coloured according to the orientation of the studied phase relative to the sample surface, allowing the differentiation of phase orientations. Finally, microstructural data are plotted on pole figures to allow the stereographic projection of crystallographic ORs of baddeleyite to be observed.

2.2.2. SIMS analysis

Following EBSD analyses, samples were mounted alongside baddeleyite reference materials Phalaborwa and FC4b (Heaman and LeCheminant, 1993; Heaman, 2009; Chamberlain et al., 2010) and gold coated for SIMS analysis. *In-situ* U-Pb analysis were undertaken using the CAMECA IMS 1280-HR ion microprobe at the Heidelberg Ion Probe (HIP) facility at the Institute of Earth Sciences, Heidelberg University. A 0.5 nA $^{16}O^-$ primary beam was focused to ~5 μm, with secondary ions extracted at 10 kV. The ion microprobe was tuned to a mass resolution (M/ΔM; 10% peak height) of ~4650 to resolve interferences from REEs and Hf oxides. 1×10^{-5} mbars of O_2 were bled into the sample chamber for enhanced Pb^+ ionization and suppression of orientation effects (*e.g.,* oxygen flooding; Schmitt et al., 2010; Chamberlain et al., 2010). Isotopes $^{90}Zr_2O^+$, $^{204}Pb^+$, $^{206}Pb^+$, $^{207}Pb^+$, $^{208}Pb^+$, $^{232}Th^+$, $^{238}U^+$, $^{238}UO^+$ and $^{238}UO_2^+$ were measured for the counting times shown in Supplementary Table A.1, using an on-axis ion counter in single collection mode. Ion counter noise was analysed in each analysis cycle. Individual analyses con-

Table 1
Analytical set up of EBSD measurements undertaken at the University of Portsmouth.

Instrumentation	
SEM Model	Zeiss EVO MA10 LaB_6 (University of Portsmouth)
EBSD system	Oxford Instruments Nordlys-nano EBSD detector
EBSD software	Oxford Instruments AZtec and HKL Channel 5
SEM set up	
Carbon coat	None
Accelerating Voltage (kV)	20
Beam current (nA)	1.5–2
Tilt (°)	70
Working distance (mm)	~14
EBSD data collection and processing	
Step size (nm)	50–100
Hough Resolution	70
Collection time per frame (ms)	<120
Background (frames)	80
EBSP noise reduction (binning)	2 × 2
EBSP noise reduction (gain)	Low
Band detection min/max	8
Baddeleyite match unit	Kudoh et al. (1986)
Raw data noise correction	Wildspike and pixel mis-indexing (level 8)

sisted of 40 seconds of pre-sputtering for removal of surface Pb contamination, and up to 20 cycles of collection for both reference materials and sample unknowns. Due to their small size, many sample unknowns ran for significantly fewer cycles due to sputtering through the baddeleyite crystal.

Isotopic data was reduced following the methodology of Chamberlain et al. (2010) and Schmitt et al. (2010). U/Pb elemental fractionation was calibrated using the power relationship between $^{206}Pb/^{238}U$ and UO_2^+/U^+ of reference materials Phalaborwa and FC4b. Analyses of Phalaborwa yielded a non-radiogenic Pb (U/Pb = 0; herein referred to as common Pb) corrected weighted mean ^{207}Pb-^{206}Pb age of 2063 ± 3 Ma (MSWD 1.7; 95% confidence) and common Pb corrected weighted mean ^{206}Pb-^{238}U age of 2053 ± 15 Ma (MSWD 0.75; 95% confidence). These values are in good agreement with previous thermal ionization mass spectrometry (TIMS) and SIMS ages (Heaman and LeCheminant, 1993; Heaman, 2009; Chamberlain et al., 2010; Schmitt et al., 2010). FC4b yielded common Pb corrected weighted mean ages of 1096 ± 10 Ma (MSWD 1.2; 95% confidence) for ^{207}Pb-^{206}Pb and 1100 ± 7 Ma (MSWD 0.6; 95% confidence) for ^{206}Pb-^{238}U, again in excellent agreement with published values (Chamberlain et al., 2010). Whilst these reference materials represent good isotopic standards, their variable U concentrations (Heaman, 2009) means absolute U concentrations were not calculated.

Due to overlap with surrounding phases and geologically young ages, martian baddeleyite analyses typically yield a $^{206}Pb/^{204}Pb$ ratio of <200; this results in large uncertainties when using traditional methods of common Pb correction using measured ^{204}Pb. We therefore analyse results using uncorrected $^{238}U/^{206}Pb$ and $^{207}Pb/^{206}Pb$ isotopic ratios on Tera-Wasserburg concordia diagrams. Cogenetic baddeleyite that have not experienced U-Pb isotopic disturbance will plot along an array denoting mixing between common and radiogenic Pb isotopic end-members; the isotopic composition of these reservoirs are therefore defined by the upper and low intercept of the discordia, respectively (Ludwig, 1998; Schoene, 2014). Additionally, cogenetic analyses with concordant U-Pb isotope systematics must define a line within $^{238}U/^{206}Pb$-$^{207}Pb/^{206}Pb$-$^{204}Pb/^{206}Pb$, allowing determination of the $^{206}Pb/^{204}Pb$ and $^{207}Pb/^{204}Pb$ of common Pb. Thus, plotting of a 3D linear regression (a Total Pb/U Isochron) provides additional common Pb isotopic constraints and results in greater precision of the determined radiogenic age than a traditional 2D Tera-Wasserburg plot (Ludwig, 1998; Schoene, 2014). These data are shown within Supplementary Fig. A.5.

3. RESULTS

3.1. Baddeleyite physical characteristics and location

Micro-baddeleyite is abundant in all samples, with more than a hundred ≥1 μm grains identified in NWA 8679 (~300 mm^2) and Zagami (~600 mm^2). The coarsest and most equant baddeleyites are observed within medium-grained NWA 7257, where the largest measures 15 μm by 7.8 μm (Fig. 2a). Baddeleyites are largely observed enclosed within or associated with late-stage phases, including ilmenite, phosphates (both merrillite and Cl-apatite), ulvöspinel, Fe-sulphide, rare fayalite, and areas of Si- and K-rich mesostasis (Fig. 2). Baddeleyite is more rarely observed enclosed within clinopyroxene, and at the boundaries between clinopyroxene and maskelynite.

3.2. Baddeleyite microstructures

A total of 31 baddeleyites were analysed using EBSD within NWA 7257 (n = 16), NWA 8679 (n = 10) and Zagami (n = 5). While baddeleyite shows no internal textural variability in BSE, EBSD analysis reveals significant inter- and intra-grain microstructural heterogeneity. Here,

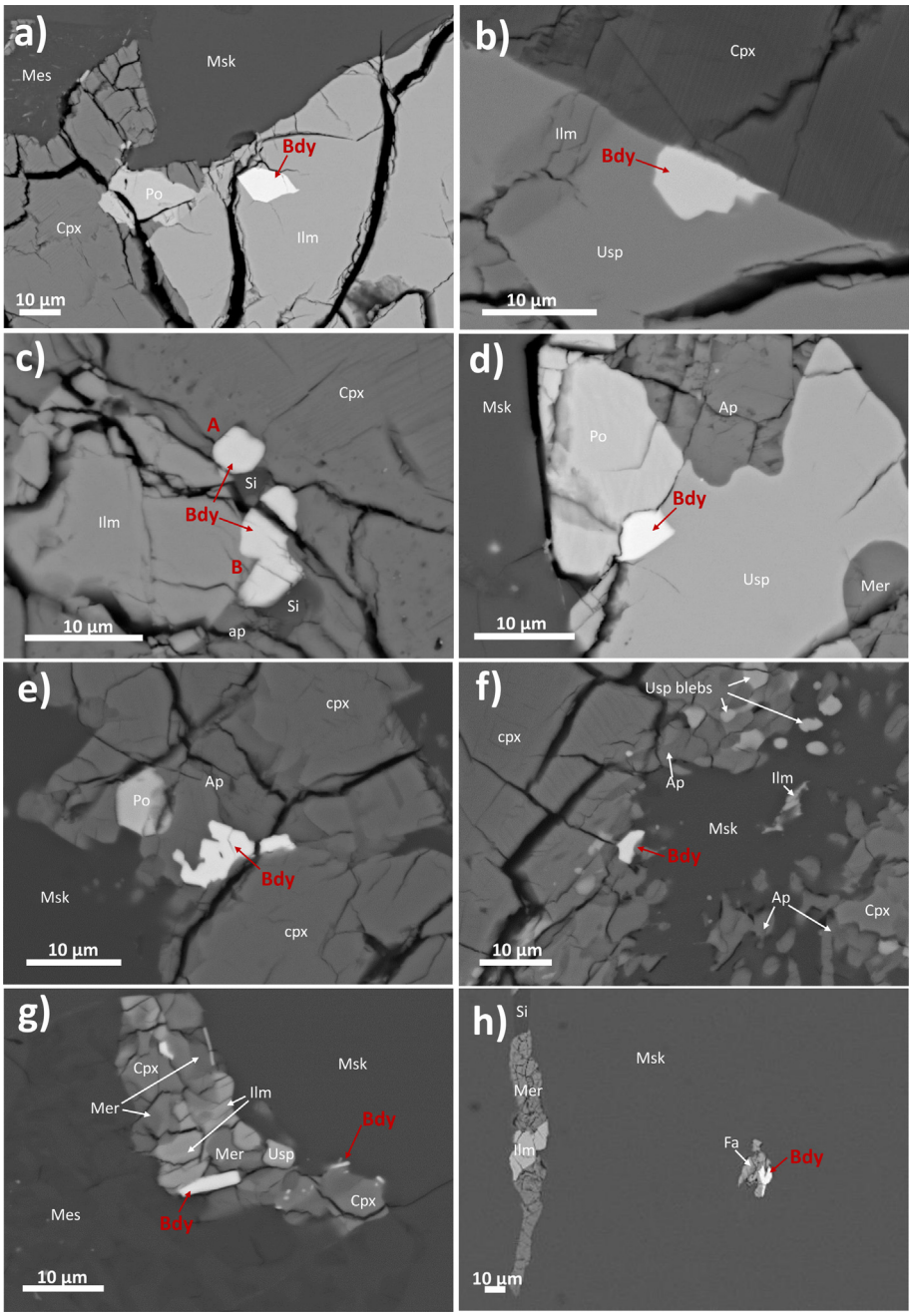

Fig. 2. Petrographic context of baddeleyite (**Bdy**) within NWA 7257, NWA 8679 and Zagami. (**a)–(c)** Baddeleyite enclosed within or in association with ilmenite (**Ilm**) or ulvöspinel (**Usp**), often adjacent to clinopyroxene (**Cpx**) or maskelynite (**Msk**). Note porous cpx rims in (c), likely indicating disequilibrium of cpx with later-stage melt that formed baddeleyite, Cl-apatite (**Ap**) and a Si-rich phase (now glass; **Si**). (**d)–(e)** Baddeleyite associated with phosphates Cl-apatite and merrillite (**Mer**) and/or pyrrhotite (**Po**). (**f)–(h)** Typically finer baddeleyite associated with maskelynite and late forming phases such as mesostasis (**Mes**) and fayalite (**Fa**). Note the abundance of sub-micron baddeleyite (brightest) within (g), which is commonly observed within NWA 8679.

we outline four broad groupings defined by similar microstructural characteristics; the variable microstructural response of baddeleyite to shock metamorphism results in a continuum of microstructures and so groupings should not be considered absolute. Where multiple microstructural domains are present within an individual grain, the dominant structural component (>50% of the baddeleyite) dictates its assigned grouping.

3.2.1. Group 1; Zagami (n = 1), NWA 7257 (n = 1), and NWA 8679 (n = 2)

A small proportion of studied baddeleyite diffract well and yield simple microstructures, with a single orientation or orientations indicative of magmatic twinning (Fig. 3a-b; Smith and Newkirk, 1965). As shown by pole figures in Fig. 3b, twin domains in NWA 7257 baddeleyite_12 possesses a common ⟨001⟩ with a 90° rotation in ⟨100⟩ and

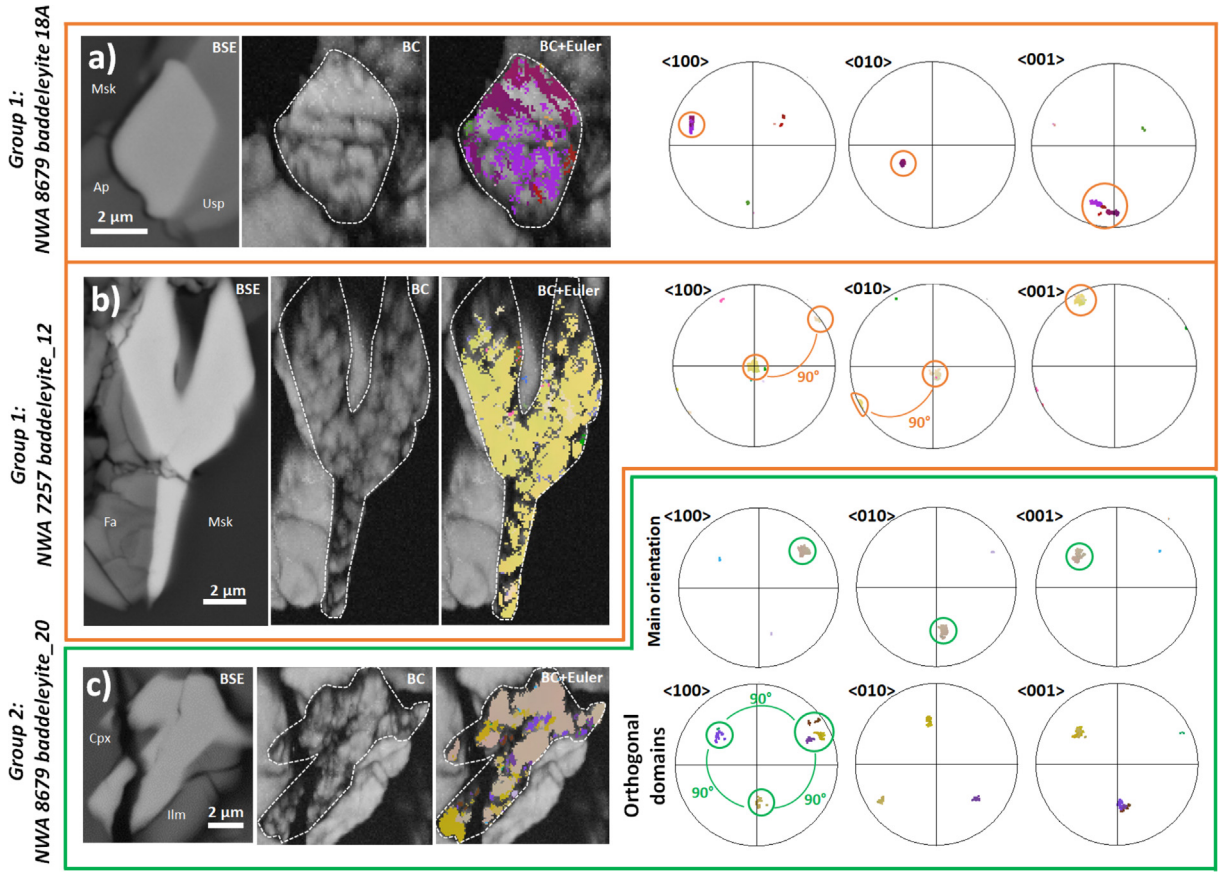

Fig. 3. Electron backscatter diffraction (EBSD) maps and pole figures for Group 1 and Group 2 baddeleyites. (a) Group 1 NWA 8679 baddeleyite_18A, which yields twin domains with a common ⟨100⟩ and ⟨010⟩, and a 18° rotation in ⟨001⟩, consistent with 180°/⟨100⟩ twin relationships. Very localised areas of phase reversion are shown by red and green clusters (coloured to Euler maps) within pole figures. **(b)** Group 1 NWA 7257 baddeleyite_12; on pole figures twin domains possess a common ⟨001⟩ and a 90° rotation in ⟨100⟩ and ⟨010⟩, consistent with 180°/⟨001⟩ twins. An example of Group 2 baddeleyites is shown by (c) NWA 8679 baddeleyite_20. The dominant orientation hosts domains that form three, orthogonally orientated clusters on pole figures. This is indicative of partial reversion from *o*-ZrO_2. **Usp**; ulvöspinel, **Msk**; maskelynite, **Ap**; Cl-apatite; **Fa**; fayalite. **Cpx**; clinopyroxene, **Ilm**; ilmenite. (For interpretation of the references to colour in this figure legend, the reader is referred to the web version of this article.)

⟨010⟩; these orientations are consistent with 180°/⟨001⟩ magmatic twin relationships (e.g., White et al., 2018). We classify these baddeleyite into Group 1, which are defined as baddeleyite that retain relict magmatic twins and have thus experienced minimal microstructural response to shock metamorphism. Evidence of deformation is still apparent within Group 1 baddeleyites, with up to 12° of cumulative misorientation (rotation of crystallographic structure from a user-defined point) across the grain indicative of significant crystal-plastic deformation (CPD; Fig. 3a).

3.2.2. Group 2; NWA 7257 (n = 4), and NWA 8679 (n = 4)

Increased microstructural complexity is shown by a number of baddeleyite grains within NWA 7257 and NWA 8679. These baddeleyite generally diffract well, and display a dominant orientation that has up to 20° of crystal-plastic deformation. In contrast to Group 1, baddeleyites possess subdomains related by orthogonal ORs, as shown in Fig. 3c. These subdomains are often observed at the edge of the baddeleyite; within NWA 7257 two examples yield apparent discontinuous rims of orthogonally related domains (Supplementary Fig. A.3). While Group 2 baddeleyite represent 40% and 25% of studied baddeleyite within NWA 8679 (*total* = 10) and NWA 7257 (*total* = 16), respectively, microstructurally comparable baddeleyite have not been recorded within Zagami. However, this may reflect the small number of baddeleyites analysed.

3.2.3. Group 3; Zagami (n = 4), NWA 7257 (n = 11), and NWA 8679 (n = 2)

A significant number of baddeleyite within NWA 7257 and Zagami, and a smaller proportion of baddeleyite within NWA 8679, have significantly lower overall diffraction intensities in comparison to previously described baddeleyite, and are classified into Group 3 (Fig. 4a-b). A decrease in BC intensity is observed despite strong diffraction of surrounding phases, demonstrating a good local surface polish quality. Within each grain, BC images reveal complex nanostructures, with only localised domains

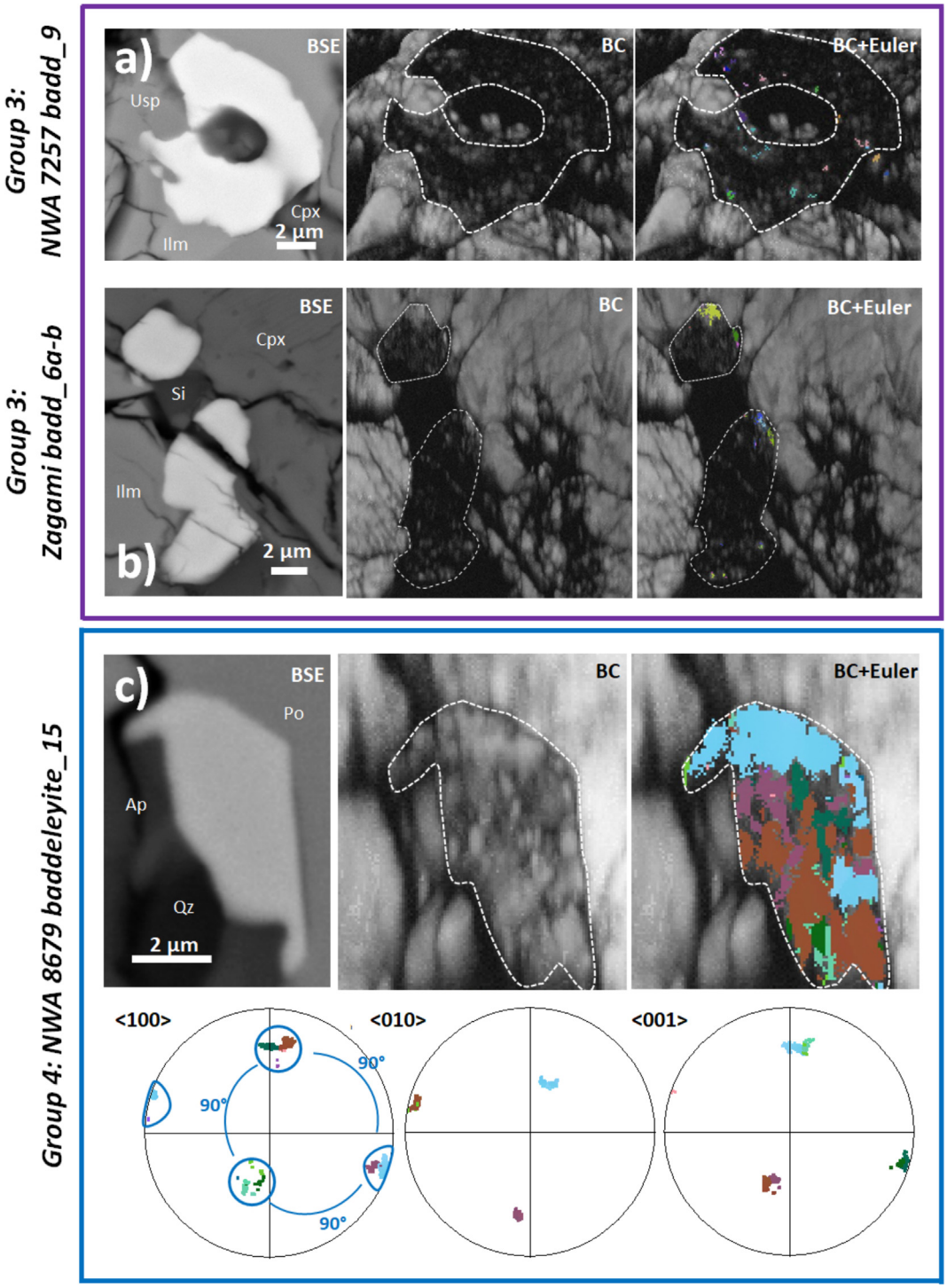

Fig. 4. Electron backscatter diffraction (EBSD) maps and pole figures for Group 3 and Group 4 baddeleyites. Quasi-amorphous baddeleyite within Group 3 shown by (**a**) NWA 7257 baddeleyite_9 and (**b**) Zagami baddeleyite_5A and 5B. Pole figures are not shown for this grouping, as the decrease in crystallinity results in a low degree of indexing of *m*-ZrO_2 during EBSD analysis. Group 4 baddeleyites are shown by (**c**) NWA 8679 baddeleyite_15, with pole figures showing three, orthogonally related *m*-ZrO_2 clusters indicative of reversion from *o*-ZrO_2. Charging during EBSD analysis has resulted in a slight *in-run* shift. **Usp;** ulvöspinel, **Cpx;** clinopyroxene, **Ilm;** ilmenite, **Si;** silica glass, **Po;** pyrrhotite, **Ap;** Cl-apatite; **Qz;** quartz.

displaying simple or orthogonal ORs separated by areas of poor microstructural ordering. Group 3 baddeleyites are microstructurally analogous to zirconia grains in NWA 5298 that are quasi-amorphous at EBSD length scales (≤50 nm), but variably ordered at the nanoscale (Darling et al., 2016).

3.2.4. Group 4; NWA 8679 (n = 2)

Two baddeleyites within NWA 8679 yield distinct, orthogonally related subdomains across the bulk of the crystal, separated by areas of degraded crystallinity (Fig. 4c). These baddeleyite are classified into Group 4, and are unique to NWA 8679 within this study. Microstructural data are not tightly clustered, indicating processes of deformation were active during the generation of Group 4 microstructures. While crystallinity of NWA 8679 baddeleyite_28 is degraded where adjacent to maskelynite (Supplementary Fig. A.4), NWA 8679 baddeleyite_15 yields strong diffraction across the entire grain (Fig. 4c).

3.3. SIMS results

In total, thirty-two *in-situ* U-Pb isotopic analyses of baddeleyite were conducted in this study (Table 2), including targets in Zagami ($n = 5$), NWA 7257 ($n = 17$) and NWA 8679 ($n = 10$). Twenty-seven of the measured baddeleyite were previously analysed using EBSD, with baddeleyite from microstructural Groups 1–3 represented within U-Pb measurements. Group 4 baddeleyites were deemed too fine grained for SIMS analysis, and thus the effects of shock on U-Pb systematics within this grouping have not been investigated. *In-situ* U-Pb isotopic analyses of NWA 7257, NWA 8679 and Zagami baddeleyite yielded $^{238}U/^{206}Pb$ ratios of 1.190–36.390 and $^{207}Pb/^{206}Pb$ isotopic ratios of 0.0753–0.8094 (Fig. 5). The proportion of radiogenic ^{206}Pb within analyses ranges from 3% to 97%, with only a single measurement yielding $^{206}Pb/^{204}Pb$ of >500.

U-Pb isotopic analyses of NWA 7257 baddeleyite define a discordia with a lower intercept age of 195 ± 15 Ma (95% confidence), and an upper intercept $^{207}Pb/^{206}Pb$ of 0.912 ± 0.068 (95% confidence; Fig. 5a); the mean square weighted deviation (MSWD) of this regression of 5.6 ($n = 17$). The upper intercept is less radiogenic than the $^{207}Pb/^{206}Pb$ weighted mean (0.998 ± 0.053; 95% confidence) of NWA 7257 maskelynite and clinopyroxene (determined by LA-ICP-MS; Supplementary Fig. A.6). The weighted mean of ^{207}Pb-corrected ages, calculated using upper intercept $^{207}Pb/^{206}Pb$ 0.912, is 187 ± 13 Ma (95% confidence, MSWD 4.6; Fig. 6a), which is within uncertainty of the discordia age. There is no link between U-Pb isotope systematics and microstructural groupings, with the greatest control on U-Pb isotopic compositions reflecting baddeleyite grain size and overlap with surrounding phases. The singular example of potential microstructural control on U-Pb isotopic compositions is shown by baddeleyite_6 (Table 2), where the poorly diffracting portion of the crystal is ~16 Myr younger than the indexing domain. These measurements are within uncertainty, and so any isotopic disturbance cannot be resolved at the resolution of these analyses.

Uncorrected U-Pb isotopic analysis of baddeleyite within NWA 8679 also form a discordia, resulting in a lower intercept age of 220 ± 23 Ma (95% confidence; MSWD 2.2, $n = 10$) and upper intercept $^{207}Pb/^{206}Pb$ of 0.788 ± 0.080 (95% confidence; Fig. 5b). The upper intercept is significantly less radiogenic than the common Pb $^{207}Pb/^{206}Pb$ weighted mean (1.057 ± 0.051; 95% confidence) of maskelynite and clinopyroxene (determined by LA-ICP-MS; Supplementary Fig. A.6). Baddeleyite U-Pb isotopic analyses within NWA 8679 possess a greater spread of U-Pb isotopic compositions than NWA 7257, though no analyses possess >90% radiogenic ^{206}Pb (Table 2). This reflects the smaller grain size of NWA 8679 baddeleyite and subsequent increased overlap with surrounding phases; despite higher counts for both U and Pb than within NWA 7257, this often results in larger analytical uncertainties for individual measurements. ^{207}Pb-corrected ages, calculated using the upper intercept $^{207}Pb/^{206}Pb$ 0.788, yield a weighted mean of 215 ± 17 Ma (95% confidence, MSWD 1.5, $n = 10$; Fig. 6b). NWA 8679 baddeleyite_29 (194 ± 751 Ma) and baddeleyite_35 (−22 ± 336 Ma) are included in the calculation of the weighted mean, but excluded from Fig. 6b for clarity, as the low percentage of radiogenic ^{206}Pb within these analyses results in substantial ^{207}Pb-corrected age uncertainties. As for NWA 7257, there is no clear link between baddeleyite microstructure and U-Pb isotopic composition.

Four >25 μm^2 baddeleyites within Zagami were analysed for U-Pb isotope systematics, with two analyses undertaken of baddeleyite_2 (Fig. 5c). Most analyses are within uncertainty of the regression reported by Zhou et al. (2013); however, the most radiogenic measurement plots below the error envelope of the discordia, yielding lower $^{238}U/^{206}Pb$ for the same $^{207}Pb/^{206}Pb$ of Zhou et al. (2013). Regression of our measurements results in a lower intercept age of 229 ± 16 Ma and upper intercept $^{207}Pb/^{206}Pb$ of 0.91 ± 0.05 (both 95% confidence; MSWD 1.12, n = 5). Given the low number of analyses, this regression is not shown on Fig. 5c. Baddeleyite within Zagami is dominantly classified within Group 3, yet microstructure again shows no link with the U-Pb isotopic composition of measurements.

4. DISCUSSION

4.1. Baddeleyite microstructure

While previous studies of baddeleyite within shergottites, including Zagami, have argued for an absence of phase transformations on the basis of Raman spectroscopy (Niihara, 2011; Niihara et al., 2012; Zhou et al., 2013; Wu et al., 2021), our microstructural results document widespread reversion from high P-T zirconia polymorphs in studied samples. This is shown by *m*-ZrO_2 domains linked by orthogonal ORs, reflecting reversion from meta-stable orthorhombic or tetragonal zirconia polymorphs. The low peak- and post-shock temperatures experienced by Zagami and shergottites with comparable bulk shock characteristics (≤220 °C; Malavergne et al., 2001; Fritz et al., 2005; Stöffler et al., 2018) strongly argue that baddeleyite microstructures document reversion from orthorhombic zirconia (*o*-ZrO_2); except in localised areas of shock melting, it is highly unlikely that post-shock temperatures reached the ~1170 °C required to induce transformation to tetragonal zirconia (*t*-ZrO_2). However, widespread reversion from *o*-ZrO_2 is expected given that material ejected from Mars likely experienced minimum shock pressures of ~5 GPa (Fritz et al., 2005), which is in excess of pressures (≥3.3 GPa; Takagi

Table 2
U-Pb isotope systematics of baddeleyite from Zagami, NWA 7257 and NWA 8679. ^{207}Pb-corrected ages calculated using the following common Pb ^{207}Pb/^{206}Pb ratios: Zagami (0.93 ± 0.19; Zhou et al., 2013), NWA 7257 (0.912 ± 0.068; this study) and NWA 8679 (0.788 ± 0.080; this study). *na;* not analysed for microstructural grouping.

Sample	Baddeleyite	Microstructure	^{238}U/^{206}Pb	2σ	^{207}Pb/^{206}Pb	2 σ	^{204}Pb/^{206}Pb	2 σ	^{207}Pb-corrected Age (Ma)	2 σ	^{206}Pb$_r$%	UO_2/U
NWA 7257	4	Group 3	10.873	1.714	0.6899	0.1008	0.0272	0.0166	151	80	26	4.10
NWA 7257	5	Group 3	26.151	1.662	0.1183	0.0141	0.0082	0.0054	223	15	92	5.40
NWA 7257	6-1	Group 2	34.892	2.070	0.0753	0.0102	0.0018	0.0018	177	11	97	4.93
NWA 7257	6-2	Group 3	36.390	2.452	0.1198	0.0204	0.0059	0.0039	161	12	92	4.55
NWA 7257	7	Group 2	23.821	7.851	0.2881	0.0763	0.0119	0.0158	193	67	72	4.10
NWA 7257	8	Group 3	9.363	2.432	0.6307	0.1389	0.0464	0.0354	220	127	33	4.22
NWA 7257	9	Group 3	20.313	2.405	0.3199	0.0393	0.0305	0.0147	214	30	69	4.21
NWA 7257	12	Group 1	4.675	0.719	0.8094	0.0186	0.0635	0.0110	159	102	12	3.60
NWA 7257	13	Group 2	5.074	1.551	0.6973	0.0644	0.0447	0.0185	308	149	25	4.60
NWA 7257	14	Group 3	24.474	1.802	0.1968	0.0325	0.0168	0.0113	215	19	83	6.79
NWA 7257	15	Group 3	12.274	1.681	0.6742	0.1156	0.0396	0.0299	142	78	28	4.57
NWA 7257	17	Group 3	25.069	4.366	0.2136	0.0822	0.0058	0.0116	205	43	81	5.94
NWA 7257	20	Group 2	10.266	2.219	0.6315	0.0832	0.0483	0.0315	200	80	33	4.99
NWA 7257	22	*na*	20.969	2.676	0.3739	0.0362	0.0259	0.0090	189	28	62	5.55
NWA 7257	18A	Group 3	9.606	1.099	0.5991	0.0338	0.0447	0.0211	238	50	36	3.87
NWA 7257	18B	Group 3	24.950	4.753	0.2190	0.0446	0.0119	0.0116	204	41	80	3.96
NWA 7257	21A	Group 3	23.261	1.809	0.3480	0.0241	0.0247	0.0112	179	17	65	6.25
NWA 8679	1	*na*	23.315	2.204	0.1483	0.0228	0.0089	0.0026	236	24	87	4.98
NWA 8679	11i B	Group 3	25.432	3.175	0.1371	0.0268	0.0088	0.0038	220	29	89	5.55
NWA 8679	11i D	Group 2	25.833	2.424	0.2020	0.0172	0.0101	0.0030	195	20	80	4.82
NWA 8679	14	Group 2	5.252	2.304	0.6383	0.0817	0.0444	0.0120	245	198	23	3.21
NWA 8679	18	Group 1	14.335	3.429	0.3868	0.0531	0.0243	0.0133	240	68	56	5.21
NWA 8679	20	Group 2	9.569	2.500	0.4864	0.0701	0.0284	0.0065	270	102	43	7.36
NWA 8679	24	*na*	8.842	2.131	0.5040	0.0376	0.0373	0.0148	275	88	41	3.39
NWA 8679	29	Group 2	1.190	1.147	0.7611	0.0662	0.0523	0.0168	194	751	7	2.70
NWA 8679	35	*na*	2.956	0.616	0.7956	0.0804	0.0489	0.0147	−22	336	3	4.29
NWA 8679	44	*na*	20.379	2.837	0.3066	0.0696	0.0170	0.0062	203	42	66	4.09
Zagami	2-1	Group 1	3.912	0.742	0.7889	0.0417	0.0371	0.0181	259	303	16	11.90
Zagami	2-2	Group 3	5.485	0.584	0.7019	0.0841	0.0427	0.0181	298	213	26	11.48
Zagami	4	Group 3	22.056	4.055	0.2084	0.0304	0.0065	0.0044	236	45	82	4.28
Zagami	5B	Group 3	17.603	1.632	0.4050	0.0299	0.0297	0.0105	215	39	60	3.56
Zagami	6A	Group 3	24.832	2.183	0.1141	0.0067	0.0055	0.0020	237	21	93	3.77

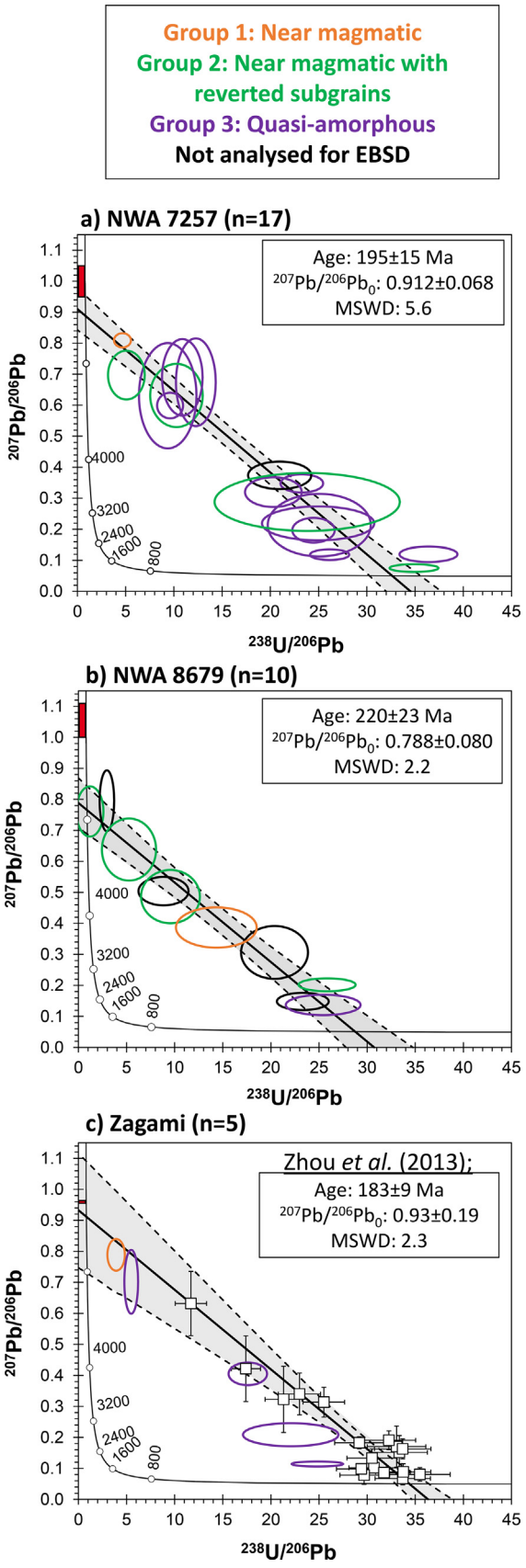

et al., 2020) required to facilitate transformation to *o*-ZrO_2 at ambient temperatures. Raman spectroscopy therefore cannot resolve reversion history, and so should not be used in isolation to investigate baddeleyite phase heritage.

Despite complete conversion of plagioclase to diaplectic glass within all studied samples, typically indicating bulk shock pressures of ≥28 GPa (Stöffler et al., 2018), the preservation of baddeleyite with magmatic twin relationships are also observed. Comparable inter- and intragrain variability has been recorded by previous microstructural analyses of shocked baddeleyite (Darling et al., 2016; White et al., 2018). However, the association of baddeleyite with magmatic twinning and phases of high shock impedance documented within NWA 5298 (Darling et al., 2016) is not as clearly resolved within the samples studied here. For example, NWA 7257 baddeleyite_12 represents the least modified crystal within this study (Fig. 3b), yet is in direct contact with plagioclase (now diaplectic glass), a phase of low shock impedance. Nevertheless, studied samples preserve both primary structural features of magmatic baddeleyite and evidence of widespread phase reversion, a testament to micron-scale shock wave heterogeneity during ejection from the martian surface (Sharp and DeCarli, 2006).

Partial to complete reversion from *o*-ZrO_2 is observed within Groupings 2–4, with variation in post-shock temperature likely controlling the degree of nucleation of reverted *m*-ZrO_2. Degraded crystallinity of baddeleyite is apparent within all samples, reflecting inhibited nucleation of *m*-ZrO_2 crystallites at length scales below the resolution of our EBSD analyses (<50 nm) during reversion of zirconia polymorphs under low post-shock temperatures (*e.g.*, Darling et al., 2016; White et al., 2018). The dominance of quasi-amorphous baddeleyite (Group 3) within NWA 7257 and Zagami is in agreement with calculated low post-shock temperatures of ~70 °C to ~220 °C for Zagami (Stöffler et al., 1986; Nyquist et al., 2001; Fritz et al., 2005). Low post-shock temperatures are also suggested by Zagami phosphates, which, despite large uncertainties, yield a ^{238}U-^{206}Pb age of 153 ± 81 Ma (2σ; Zhou et al., 2013). This is in good agreement with other isotopic systems and indicates negligible U-Pb open-system behaviour (≤400 °C; Chew and Spikings, 2015).

Fig. 5. Tera-Wasserburg diagram showing uncorrected U-Pb isotopic measurements of baddeleyite. Ellipses denote 2σ uncertainties, and are coloured relative to microstructural grouping. Generated in Isoplot (Ludwig, 2003); all intercept uncertainties reported at 95% confidence intervals. Weighted mean of common Pb $^{207}Pb/^{206}Pb$ shown in red; $^{207}Pb/^{206}Pb$ isotopic ratios determined by LA-ICP-MS for NWA 7257 and NWA 8679, while values for Zagami are from Bellucci et al. (2015). **(a)** Discordia regression of baddeleyite within NWA 7257. **(b)** Discordia regression of baddeleyite within NWA 8679. **(c)** Zagami; measurements within this study (ellipses) plotted with data and discordia regression from Zhou et al. (2013). (For interpretation of the references to colour in this figure legend, the reader is referred to the web version of this article.)

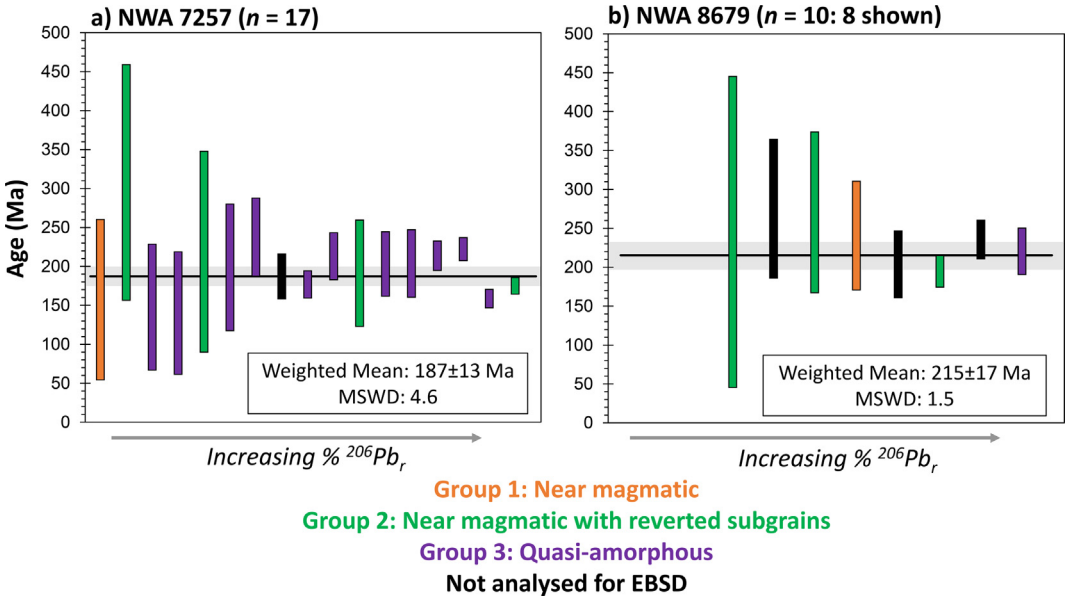

Fig. 6. Weighted means of ^{207}Pb-corrected ages of baddeleyite within (**a**) NWA 7257 and (**b**) NWA 8679. Data are coloured according to microstructural grouping and plotted with increasing proportions of radiogenic ^{206}Pb. NWA 8679 baddeleyite_29 and baddeleyite_35 are included in the generation of the weighted mean, but excluded from (b) for clarity. Figures generated using Isoplot (Ludwig, 2003); weighted mean uncertainties reported to 95% confidence intervals. (For interpretation of the references to colour in this figure legend, the reader is referred to the web version of this article.)

Complete transformation and reversion under sufficient magnitude and longevity of post-shock temperatures to nucleate micron-scale *m*-ZrO_2 is shown by Group 4 grains. These grains are uncommon, constituting 20% of NWA 8679 baddeleyite and completely absent in NWA 7257 and Zagami; their higher abundance in NWA 8679 compared to other microstructural groupings likely indicates heterogeneous magnitude and longevity of post-shock heating. Some control from the thermal properties of surrounding phases is also apparent; where in contact with crystalline apatite and clinopyroxene, significant nucleation of *m*-ZrO_2 is observed in NWA 8679 baddeleyite_28 (Supplementary Fig. A.4), yet this ordering is lost towards the contact with diaplectic glass. While these microstructures do not constitute the bulk microstructure of any studied baddeleyites within NWA 7257 and Zagami, greater nucleation of *m*-ZrO_2 caused by localised amplification of shock pressures and/or temperatures focused at the interface between igneous phases may be shown by the presence of reverted 'rims' in NWA 7257 and Zagami (Supplementary Fig. A.3). Importantly, baddeleyites in NWA 7257, NWA 8679 and Zagami lack distinct granular domains or zircon rims (Darling et al., 2016), indicating that even where elevated post-shock temperatures occur, they are of insufficient magnitude to generate many of the observed baddeleyite microstructures in NWA 5298.

4.2. Linking baddeleyite microstructure and U-Pb isotopic compositions

4.2.1. Discordia ages and ^{207}Pb-corrected ages

Baddeleyite form well constrained discordia within Tera-Wasserburg diagrams, reflecting restricted radiogenic Pb ingrowth and incorporation of Pb from surrounding phases during analysis of ≤5 μm grains. Discordia ages of 195 ± 15 Ma and 220 ± 23 Ma (95% confidence; Fig. 5) for NWA 7257 and NWA 8679, respectively, are in line with the previously determined range of ages (ca. 225–160 Ma) for enriched shergottites (Nyquist et al., 2001; Moser et al., 2013; Zhou et al., 2013; Udry et al., 2020; Váci and Agee, 2020). Some scatter of U-Pb isotopic data near the concordia is apparent (NWA 7257 and Zagami; Fig. 5). This likely reflects crystal orientation effects, which are well documented within baddeleyite (Wingate and Compston, 2000) and can be dampened but not fully negated by oxygen flooding (Schmitt et al., 2010). As sufficient isotopic measurements were undertaken within NWA 7257 ($n = 17$), isotopic compositions that fall below the discordia (*e.g.,* baddeleyite_5) do not impact the calculated age.

Within Zagami, with the most radiogenic analysis (baddeleyite_6A) yields resolvably lower ^{238}U/^{206}Pb than analyses with comparable ^{207}Pb/^{206}Pb reported by Zhou et al. (2013). This data point strongly weights any regression of Zagami U-Pb isotopic data, and results in a lower intercept age of 229 ± 16 Ma that falls outside of uncertainty of the Zhou et al. (2013) reported age of 182.7 ± 6.9 Ma. We suggest the lower ^{238}U/^{206}Pb could again be symptomatic of orientation effects, which any regression of our Zagami U-Pb isotopic analyses are susceptible to due to the low number of measurements (n = 5). Additional considerations may be the different matrices of poorly-diffracting, nano-structurally complex martian baddeleyites and crystalline RMs, and localised orientation effects in RMs; we note that while RMs bracketing Zagami measurements yield consistent UO_2/U, they show minor reverse

discordance that likely reflects analytical scatter in Pb/U relative sensitivity and thus the U-Pb calibration (*e.g.,* Schmitt et al., 2010). Given the prevalence of quasi-amorphous baddeleyite microstructures within our studied sample, it seems unlikely that those reported within Zhou et al. (2013) differ significantly microstructurally. Thus, while matrix effects are an important consideration for future studies of shocked baddeleyite, it is unlikely that such effects account for the observed difference between radiogenic U-Pb analyses. Localised orientation effects in both sample unknowns and RMs, magnified by a low number of analyses, may therefore account for the lower $^{238}U/^{206}Pb$ of radiogenic baddeleyite_6A, and thus discrepancies in the discordia lower intercept of this study and that of Zhou et al. (2013). These data highlight the requirement for sufficient isotopic analyses, but also show that observed U-Pb isotopic variability within radiogenic baddeleyite (>90% radiogenic ^{206}Pb) of NWA 7257 and Zagami may be explained by analytical effects, rather than reflecting U-Pb isotopic disturbance.

Upper intercept $^{207}Pb/^{206}Pb$ indicates that common Pb isotopic compositions within both NWA 7257 and NWA 8679 represent mixtures of martian (enriched shergottite common Pb $^{207}Pb/^{206}Pb$ typically >0.95; Bellucci et al., 2015) and modern terrestrial reservoirs (modern $^{207}Pb/^{206}Pb$ 0.836; Stacey and Kramers, 1975). The measured $^{207}Pb/^{206}Pb$ of clinopyroxene and maskelynite (Supplementary Material A) are comparable to previously reported $^{207}Pb/^{206}Pb$ of clinopyroxene and maskelynite within enriched shergottites (Moser et al., 2013; Bellucci et al., 2015), suggesting that overlap with fractures during analyses of baddeleyite exerts the greatest control on common Pb $^{207}Pb/^{206}Pb$. Importantly, while ^{207}Pb-corrected ages of analyses lowest in radiogenic ^{206}Pb are sensitive to choice of common Pb isotopic composition (*e.g.,* NWA 8679 baddeleyite_35), this terrestrial contamination has little effect on the determined lower intercept age due to the strong fit of uncorrected analyses to a discordia.

4.2.2. Microstructural constraints on U-Pb isotopic compositions

Critically, baddeleyite U-Pb isotopic compositions show no apparent relationship with observed microstructures (Figs. 5 & 6). This indicates that within the studied samples, shock metamorphism and associated zirconia phase transformation has not resulted in resolvable U-Pb isotopic disturbance at the length scales of SIMS analyses (~5 μm). The absence of age variability with baddeleyite microstructure and the presence of statistically robust discordia indicates negligible U-Pb isotopic disturbance and strongly argues that calculated ages represent the time of magmatic crystallization, rather than shock resetting as suggested by advocates for old shergottite ages (*e.g.,* Bouvier et al., 2008; El Goresy et al., 2013). Individual baddeleyites with magmatic microstructures and high proportions of radiogenic ^{206}Pb that yield late Amazonian ^{207}Pb-corrected ages in NWA 7257, NWA 8679 and Zagami are therefore unequivocal evidence of geologically young shergottites. We therefore show that both baddeleyite U-Pb analyses and other isotope systematics, including Sm-Nd, Lu-Hf, Rb-Sr and U-Pb mineral isochrons, are resilient to shock metamorphism and record magmatic events, and that *in-situ* baddeleyite U-Pb ages in NWA 7257, NWA 8679 and Zagami provide additional resolution to the shergottite age paradox (*e.g.,* Váci and Agee, 2020).

These results provide important new constraints on baddeleyite U-Pb systematics in planetary materials, resolving the contradiction between experimental studies, which show closed-system U-Pb isotope systematics up to ~57 GPa (Niihara et al., 2012), and previously documented age resetting in terrestrial and meteoritic baddeleyite (Moser et al., 2013; Darling et al., 2016; White et al., 2017). Age resetting in natural baddeleyite has been directly linked with the development of microstructures formed by reversion from high P-T zirconia polymorphs during shock metamorphism, which enhance the mobilisation potential of Pb (Darling et al., 2016; White et al., 2017, 2018). This can result in Pb diffusion at temperatures lower than required to enable significant volume diffusion in undeformed baddeleyite (>900 °C; Heaman and LeCheminant, 1993). This is documented by near complete age resetting in granular baddeleyite in shergottite NWA 5298 in areas of impact melting (Moser et al., 2013; Darling et al., 2016), shock resetting within reverted domains in Sudbury baddeleyite (White et al., 2017), and mobilisation of Pb along defect-rich nanoscale boundaries during greenschist facies metamorphism ca. 450 Myr after shock metamorphism (White et al., 2017). However, one important difference between the shergottites studied here and those from previous studies is the intensity, and likely longevity, of post-shock heating.

While shock pressures up to 57 GPa and post-shock annealing at >1000 °C did not result in disturbance of U-Pb systematics in the experimental study of Niihara et al. (2012), this likely reflects the short duration of experimental shock loading in comparison to natural samples. Though post-shock heating may be realistic, the shock pulse durations of experimental studies are an order of magnitude shorter (≤ μs) than natural shock events (≥*m*s), thus inhibiting the range of shock conditions experienced (Sharp and DeCarli, 2006; Niihara et al., 2012). Given the strong dependence of shock transformation to kinetic effects, such short shock pulses may have been insufficient to cause phase transformation of baddeleyite within the study of Niihara et al. (2012), limiting the generation of reverted microstructures and subsequent pathways for Pb loss during annealing. Contrasts between experimental and natural studies of shocked baddeleyite therefore indicate that nanostructures formed by reversion from high P-T zirconia polymorphs may facilitate U-Pb isotopic disturbance, but only at high, and likely sustained, post-shock temperatures. Consequently, it can be concluded that the shergottites studied here experienced insufficient post-shock heating to induce resolvable Pb mobility.

Thus, the dominance of microstructural Group 3 baddeleyite and independent constraints of low post-shock temperatures within Zagami (≤220 °C; Stöffler et al., 1986; Nyquist et al., 2001; Fritz et al., 2005) add considerable support to the interpretation that the previously determined baddeleyite age of 182.7 ± 6.9 Ma (Zhou et al., 2013)

represents the timing of magmatic crystallization. While some Pb loss was reported in quasi-amorphous grains in NWA 5298 (Darling et al., 2016), those with the least structural ordering yielded the least disturbed U-Pb isotopic compositions and the most robust dates. The weak diffraction of reverted domains for baddeleyite within Zagami (Fig. 4b) shows similarly poor structural ordering, indicating short time-scales of heating resulted in negligible Pb loss within these domains. We do however caution that U-Pb isotopic analyses were not undertaken on baddeleyites within microstructural group 4, which formed under post-shock temperatures sufficient to nucleate micron-scale *m*-ZrO_2 across the bulk of the grain. Such increased structural ordering may facilitate Pb loss and therefore disturb U-Pb isotope systematics. As Group 4 baddeleyites are located at distance from shock melting and NWA 8679 yields no additional petrographic evidence of increased post-shock temperatures across the bulk of the sample, the presence of microstructurally comparable baddeleyite cannot be discounted in shergottites with similar bulk shock characteristics. Thus, the magnitude of U-Pb isotopic disturbance in Group 4 grains is currently unresolved, and strongly argues for careful microstructural characterization by EBSD prior to destructive dating of baddeleyite within shergottites.

4.3. Implications for martian processes

Martian meteorites currently represent our only direct means of sampling martian crust. Thus, increased chronological and lithological diversity allows for further insights into martian crust-mantle processes, such as magmatic emplacement, subsequent crustal evolution, and aqueous alteration. Our study further expands the number of ages derived from enriched shergottites, and provides robust microstructural constraints on the significance of late Amazonian ages within the martian meteorite record. Most enriched shergottites yield ~3 Ma CREs (Udry et al., 2020) and possess crystallization ages of 220–160 Ma (*e.g.,* Nyquist et al., 2001), suggesting their derivation from the same ejection event and thus a shared source terrane. The source terrane for NWA 7257, NWA 8679 and Zagami is almost certainly a large and long-lived Amazonian volcanic province, such as examples within the Northern lowlands, including Tharsis and Elysium (Udry et al., 2020; Váci and Agee, 2020).

Importantly, while NWA 7257 yields a crystallisation age within uncertainty of both NWA 8679 and Zagami, the calculated ages of NWA 8679 (220 ± 23 Ma) and Zagami (183 ± 7 Ma; Zhou et al., 2013) indicate discrete magmatic events. Given their shared mantle source characteristics, NWA 8679 and Zagami may represent distinct but spatially-associated igneous bodies derived from the same enriched mantle reservoir, reflecting tens of Myrs of magmatic activity from an enriched mantle domain or domains (Nyquist et al., 2001; Combs et al., 2019). We tentatively suggest that subtle differences in baddeleyite microstructural characteristics between the studied samples may also reflect sampling of distinct igneous events. While Zagami and NWA 7257 baddeleyite are dominated by Group 3 microstructures, baddeleyite in ~220 Ma NWA 8679 retain a greater proportion of relict magmatic microstructures and, where transformation to *o*-ZrO_2 occurs, have largely experienced sufficient post-shock temperatures to nucleate micron-scale domains of revered *m*-ZrO_2. Though we note the CRE of NWA 8679 is unknown, thus a petrogenetic link to NWA 7257 and Zagami uncertain, and that shock wave propagation is an inherently heterogeneous process, such variation in baddeleyite microstructure may reflect lower bulk shock pressures coupled with higher (and more prolonged) post-shock temperatures during ejection from the martian surface. This may highlight sampling of different crustal domains or depths during the launch event. Regardless, our data provides increased age diversity within enriched shergottites, and highlights the requirements of a robust chronological framework to explore the secular evolution of martian magmatism, both globally and at individual magmatic centres.

5. CONCLUSIONS

We have conducted a systematic investigation of baddeleyite microstructure and *in-situ* U-Pb geochronology within three enriched shergottites: Northwest Africa (NWA) 7257, NWA 8679 and Zagami. Significant microstructural variability of baddeleyite is observed, with widespread reversion from high-pressure *o*-ZrO_2. We define four groupings on the basis of a continuum of baddeleyite microstructures, with Groups 1–4 detailing increased microstructural response of baddeleyite to greater magnitudes of shock deformation and/or post-shock temperatures. Group 3, characterised by baddeleyite with quasi-amorphous microstructures, is most abundant within NWA 7257 and Zagami, and represents inhibited nucleation of reverted *m*-ZrO_2 during rapid reversion from *o*-ZrO_2 at low bulk post-shock temperatures (Zagami; $\leq$ 220 °C). Only rarely were post-shock temperatures sufficient to nucleate micron-scale *m*-ZrO_2.

We observe no clear link between baddeleyite microstructure and U-Pb isotope systematics. These data strongly indicate that Pb mobility within shocked baddeleyite is driven by heating rather than phase transformation, and that the magnitude and longevity of post-shock temperatures experienced by the studied shergottites was insufficient to induce resolvable disturbance of U-Pb isotope systematics. Zirconia phase transformation therefore likely only induces Pb mobility when coupled with high and sustained post-shock temperatures, as indicated by pervasive shock melting and recrystallization of mineral assemblages within NWA 5298 (Darling et al., 2016). This finding resolves the apparent contradiction of shock induced baddeleyite age resetting shown between experimental and natural samples, by confirming that the magnitude and longevity of shock heating exerts the greatest control on U-Pb isotopic disturbance.

Our approach yields new robust, magmatic crystallization ages of 195 ± 15 Ma and 220 ± 23 Ma for NWA 7257 and NWA 8679, respectively, and confirms that the previously derived baddeleyite age of 182.7 ± 6.9 Ma for Zagami (Zhou et al., 2013) represents the timing of magmatic crystal-

lization. These chronological data add greater age diversity to the 225–160 Ma grouping of enriched shergottites, and highlights further young mafic magmatism on Mars. Importantly, NWA 7257, NWA 8679 and Zagami yield shock characteristics similar to most other shergottites, including complete transformation of plagioclase to diaplectic glass and only nascent shock melting. Thus, where low post-shock temperatures can be demonstrated by microstructural and independent mineralogical constraints, baddeleyite chronology provides the age of magmatic crystallization. Our approach underlines the powerful potential of baddeleyite as a robust U-Pb geochronometer in martian meteorites and broader planetary materials.

Declaration of Competing Interest

The authors declare that they have no known competing financial interests or personal relationships that could have appeared to influence the work reported in this paper.

ACKNOWLEDGEMENTS

This work was supported by Science and Technology Facilities Council grant [ST/S000291/1] to JRD. The assistance of Thomas Ludwig on the Heidelberg Ion Probe and the thin section preparation of Geoff Long are gratefully acknowledged. We thank Pierre Beck for editorial handling, as well as Arya Udry and two anonymous reviewers for highly constructive and detailed reviews.

APPENDIX A. SUPPLEMENTARY MATERIAL

Supplementary data to this article can be found online at https://doi.org/10.1016/j.gca.2021.09.034.

REFERENCES

Bellucci J. J., Nemchin A. A., Whitehouse M. J., Snape J. F., Kielman R. B., Bland P. A. and Benedix G. K. (2016) A Pb isotopic resolution to the Martian meteorite age paradox. *Earth Planet. Sci. Let.* **433**, 241–248.

Bellucci J. J., Nemchin A. A., Whitehouse M. J., Snape J. F., Bland P. and Benedix G. K. (2015) The Pb isotopic evolution of the Martian mantle constrained by initial Pb in Martian meteorites: Initial Pb in Martian Meteorites. *J. Geophys. Res. Planets* **120**, 2224–2240.

Bogard D. D. and Park J. (2008) ^{39}Ar-^{40}Ar dating of the Zagami Martian shergottite and implications for magma origin of excess ^{40}Ar. *Meteorit. Planet. Sci.* **43**, 1113–1126.

Borg L. E., Edmunson J. E. and Asmerom Y. (2005) Constraints on the U-Pb Isotopic Systematics of Mars Inferred from a Combined U-Pb, Rb-Sr, and Sm-Nd Isotopic Study of the Martian Meteorite Zagami. *Geochim. Cosmochim. Acta.* **69**, 5819–5830.

Bouvier A., Blichert-Toft J. and Albarède F. (2009) Martian meteorite chronology and the evolution of the interior of Mars. *Earth Planet. Sci. Lett.* **280**, 285–295.

Bouvier A., Blichert-Toft J., Vervoort J. D., Gillet P. and Albarède F. (2008) The case for old basaltic shergottites. *Earth Planet. Sci. Lett.* **266**, 105–124.

Bouvier A., Blichert-Toft J., Vervoort J. and Albarède F. (2005) The age of SNC meteorites and the antiquity of the Martian surface. *Earth Planet. Sci. Lett.* **240**, 221–233.

Cayron C., Douillard T., Sibil A., Fantozzi G. and Sao-Jao S. (2010) Reconstruction of the cubic and tetragonal parent grains from electron backscatter diffraction maps of monoclinic zirconia. *J. Amer. Ceram. Soc.* **93**, 2541–2544.

Chamberlain K. R., Schmitt A. K., Swapp S. M., Harrison T. M., Swoboda-Colberg N., Bleeker W., Peterson T. D., Jefferson C. W. and Khudoley A. K. (2010) In situ U-Pb SIMS (IN-SIMS) micro-baddeleyite dating of mafic rocks: Method with examples. *Precamb. Res.* **183**, 379–387.

Chew D. M. and Spikings R. A. (2015) Geochronology and thermochronology using apatite; time and temperature, lower crust to surface. *Elements* **11**, 189–194.

Combs L. M., Udry A., Howarth G. H., Righter M., Lapen T. J., Gross J., Ross D. K., Rahib R. R. and Day J. M. D. (2019) Petrology of the enriched poikilitic shergottite Northwest Africa 10169: Insight into the martian interior. *Geochim. Cosmochim. Acta* **266**, 435–462.

Darling J. R., Moser D. E., Barker I. R., Tait K. T., Chamberlain K. R., Schmitt A. K. and Hyde B. C. (2016) Variable microstructural response of baddeleyite to shock metamorphism in young basaltic shergottite NWA 5298 and improved U-Pb dating of Solar System events. *Earth Planet. Sci. Lett.* **444**, 1–12.

El Goresy A., Gillet P. h., Miyahara M., Ohtani E., Ozawa S., Beck P. and Montagnac G. (2013) Shock-induced deformation of Shergottites: Shock-pressures and perturbations of magmatic ages on Mars. *Geochim. Cosmochim. Acta* **101**, 233–262.

Fritz J., Artemieva N. and Greshake A. (2005) Ejection of Martian meteorites. *Meteorit. Planet. Sci.* **40**, 1393–1411.

Gaffney A. M., Borg L. E., Asmerom Y., Shearer C. K. and Burger P. V. (2011) Disturbance of isotope systematics during experimental shock and thermal metamorphism of a lunar basalt with implications for Martian meteorite chronology. *Meteorit. Planet. Sci.* **46**, 35–52.

Hartmann W. K. and Berman D. C. (2000) Elysium Planitia lava flows: Crater count chronology and geological implications. *J. Geophys. Res. Planets* **105**, 15011–15025.

Head J. N., Melosh H. J. and Ivanov B. A. (2002) Martian meteorite launch: high-speed ejecta from small craters. *Science* **298**(5599), 1752–1756.

Heaman L. M. (2009) The application of U-Pb geochronology to mafic, ultramafic and alkaline rocks: An evaluation of three mineral standards. *Chem. Geol.* **261**, 43–52.

Heaman L. M. and LeCheminant A. N. (1993) Paragenesis and U-Pb systematics of baddeleyite (ZrO2). *Chem. Geol.* **110**, 95–126.

Herd C. D. K., Moser D. E., Tait K., Darling J. R., Shaulis B. J. and McCoy T. J. (2017) Crystallization of baddeleyite in basaltic rocks from mars, and comparisons with the Earth, Moon, and Vesta. In *Microstructural Geochronology*. American Geophysical Union (AGU), pp. 137–166.

Herzog G. F. and Caffee M. W. (2014) 1.13 - Cosmic-ray exposure ages of meteorites. In *Treatise on Geochemistry* (eds. H. D. Holland and K. K. Turekian), second ed. Elsevier, Oxford, pp. 419–454.

Hui H., Peslier A. H., Lapen T. J., Shafer J. T., Brandon A. D. and Irving A. J. (2011) Petrogenesis of basaltic shergottite Northwest Africa 5298: Closed-system crystallization of an oxidized mafic melt. *Meteorit. Planet. Sci.* **46**, 1313–1328.

Irving A., Kuehner S., Chen G., Herd C., Tanaka R. and Gregory D. (2012) Petrologic, Elemental and Oxygen Isotopic Characterization of Highly Enriched Mafic Shergottite Northwest Africa 7257. 75th Annual Meteoritical Society Meeting. #5367 (abstr.).

Jiang Y. and Hsu W. (2012) Petrogenesis of Grove Mountains 020090: An enriched "lherzolitic" shergottite. *Meteorit. Planet. Sci.* **47**, 1419–1435.

Kelly P. M. and Rose L. R. F. (2002) The martensitic transformation in ceramics - its role in transformation toughening. *Prog. Mater Sci.* **95**, 463–557.

Kudoh H., Takeda H. and Arashi H. (1986) In situ determination of crystal structure for high pressure phase of ZrO_2 using a diamond anvil and single crystal X-ray diffraction method. *Phs. Chem. Min.* **13**, 223–237.

Langenhorst F. (2000) "Eclogitic" minerals in a shocked basaltic meteorite. *Earth Planet. Sci. Lett.* **176**, 259–265.

Ludwig K. R. (2003) *Isoplot/Ex: Special Publication No. 4*. Berkeley Geochronology.

Ludwig K. R. (1998) On the Treatment of Concordant Uranium-Lead Ages. *Geochim. Cosmochim. Acta* **62**, 665–676.

Malavergne V., Guyot F., Benzerara K. and Martinez I. (2001) Description of new shock-induced phases in the Shergotty, Zagami, Nakhla and Chassigny meteorites. *Meteorit. Planet. Sci.* **36**, 1297–1305.

McCoy T. J., Taylor G. J. and Keil K. (1992) Zagami: Product of a two-stage magmatic history. *Geochim. Cosmochim. Acta* **56**, 3571–3582.

McCoy T. J., Wadhwa M. and Keil K. (1999) New lithologies in the Zagami meteorite: evidence for fractional crystallization of a single magma unit on Mars. *Geochim. Cosmochim. Acta* **63**, 1249–1262.

Moser D. E., Chamberlain K. R., Tait K. T., Schmitt A. K., Darling J. R., Barker I. R. and Hyde B. C. (2013) Solving the Martian meteorite age conundrum using micro-baddeleyite and launch-generated zircon. *Nature* **499**, 454–457.

Niihara T. (2011) Uranium-lead age of baddeleyite in shergottite Roberts Massif 04261: Implications for magmatic activity on Mars. *J. Geophys. Res. Planets* **116**, E12008.

Niihara T., Kaiden H., Misawa K., Sekine T. and Mikouchi T. (2012) U-Pb isotopic systematics of shock-loaded and annealed baddeleyite: Implications for crystallization ages of Martian meteorite shergottites. *Earth Planet. Sci. Lett.* **341–344**, 195–210.

Nyquist L. E., Bogard D. D., Shih C.-Y., Greshake A., Stöffler D. and Eugster O. (2001) Ages and geologic histories of martian meteorites. *Space Sci. Rev.* **96**, 105–164.

Ohtaka O., Fukui H., Kunisada T., Fujisawa T., Funakoshi K., Utsumi W., Irifune T., Kuroda K. and Kikegawa T. (2001) Phase relations and equations of state of ZrO_2 under high temperature and high pressure. *Phys. Rev. B* **63** 174108.

Schmitt A. K., Chamberlain K. R., Swapp S. M. and Harrison T. M. (2010) In situ U-Pb dating of micro-baddeleyite by secondary ion mass spectrometry. *Chem. Geol.* **269**, 386–395.

Schoene B. (2014) U–Th–Pb geochronology. In *Treatise on Geochemistry*. Elsevier, pp. 341–378.

Sharp T. G. and DeCarli P. S. (2006) Shock effects in meteorites. In: Meteorites and the Early Solar System II, pp. 653–677.

Shih C.-Y., Nyquist L. E., Bogard D. D., McKay G. A., Wooden J. L., Bansal B. M. and Wiesmann H. (1982) Chronology and petrogenesis of young achondrites, Shergotty, Zagami, and ALHA77005: late magmatism on a geologically active planet. *Geochim. Cosmochim. Acta* **46**, 2323–2344.

Smith D. K. and Newkirk W. (1965) The crystal structure of baddeleyite (monoclinic ZrO_2) and its relation to the polymorphism of ZrO_2. *Acta Crystall.* **18**, 983–991.

Stacey J. S. and Kramers J. D. (1975) Approximation of terrestrial lead isotope evolution by a two-stage model. *Earth Planet. Sci. Lett.* **26**, 207–221.

Stöffler D., Hamann C. and Metzler K. (2018) Shock metamorphism of planetary silicate rocks and sediments: Proposal for an updated classification system. *Meteorit. Planet. Sci.* **53**, 5–49.

Stöffler D., Ostertag R., Jammes C., Pfannschmidt G., Gupta P. R. S., Simon S. B., Papike J. J. and Beauchamp R. H. (1986) Shock metamorphism and petrography of the Shergotty achondrite. *Geochim. Cosmochim. Acta* **50**, 889–903.

Tait K. T., Irving A. J., Nicklin R. I., Day J. M. D., Andreasen R., Kuehner S., Ziegler K., Lapen T. J. and Gregory D. A. (2015) Petrologic and isotopic charactetisation of enriched mafic shergottite Northwest Africa 8679. Lunar Planet. Sci. XLVI. Lunar Planet. Inst., Houston. #2709(abstr.)

Takagi S., Kyono A., Nozawa S., Kawai N., Inukai K., Fukaya R., Funamori N., Adachi S. and Ichiyanagi K. (2020) In situ observation of the phase transition behavior of shocked baddeleyite. *Geophys. Res. Lett.* **47**, e2020GL089592.

Timms N. E., Erickson T. M., Zanetti M. R., Pearce M. A., Cayron C., Cavosie A. J., Reddy S. M., Wittmann A. and Carpenter P. K. (2017a) Cubic zirconia in >2370 °C impact melt records Earth's hottest crust. *Earth Planet. Sci. Lett.* **477**, 52–58.

Timms N. E., Erickson T. M., Pearce M. A., Cavosie A. J., Schmieder M., Tohver E., Reddy S. M., Zanetti M. R., Nemchin A. A. and Wittmann A. (2017b) A pressure-temperature phase diagram for zircon at extreme conditions. *Earth-Sci. Rev.* **165**, 185–202.

Udry A., Howarth G. H., Herd C. D. K., Day J. M. D., Lapen T. J. and Filiberto J. (2020) What Martian Meteorites Reveal About the Interior and Surface of Mars. *J. Geophys. Res.: Planets* **125**, e2020JE006523.

Váci Z. and Agee C. (2020) Constraints on Martian Chronology from Meteorites. *Geosciences* **10**, 455.

Vistisen L., Petersen D. and Madsen M. B. (1992) Mössbauer spectroscopy showing large-scale inhomogeneity in the presumed martian meteorite Zagami. *Phys. Scr.* **46**, 94–96.

White L. F., Darling J. R., Moser D. E., Cayron C., Barker I., Dunlop J. and Tait K. T. (2018) Baddeleyite as a widespread and sensitive indicator of meteorite bombardment in planetary crusts. *Geology* **46**, 719–722.

White L. F., Darling J. R., Moser D. E., Reinhard D. A., Prosa T. J., Bullen D., Olson D., Larson D. J., Lawrence D. and Martin I. (2017) Atomic-scale age resolution of planetary events. *Nat. Comm.* **8**, 15597.

Wieler R., Huber L., Busemann H., Seiler S., Leya I., Maden C., Masarik J., Meier M. M. M., Nagao K., Trappitsch R. and Irving A. J. (2016) Noble gases in 18 Martian meteorites and angrite Northwest Africa 7812—Exposure ages, trapped gases, and a re-evaluation of the evidence for solar cosmic ray-produced neon in shergottites and other achondrites. *Meteorit. Planet. Sci.* **51**, 407–428.

Wingate M. T. D. and Compston W. (2000) Crystal orientation effects during ion microprobe U-Pb analysis of baddeleyite. *Chem. Geol.* **168**, 75–97.

Wu Y., Hsu W., Li Q.-L., Che X. and Liao S. (2021) Heterogeneous martian mantle: Evidence from petrology, mineral chemistry and in situ U-Pb chronology of the basaltic shergottite Northwest Africa 8653. *Geochim. Cosmochim. Acta* **309**, 352–365.

Wu Y. and Hsu W. (2020) Mineral chemistry and in situ U Pb geochronology of the mare basalt Northwest Africa 10597: Implications for low-Ti mare volcanism around 3.0 Ga. *Icarus* **338** 113531.

Zhou Q., Herd C. D. K., Yin Q.-Z., Li X.-H., Wu F.-Y., Li Q.-L., Liu Y., Tang G.-Q. and McCoy T. J. (2013) Geochronology of the Martian meteorite Zagami revealed by U-Pb ion probe dating of accessory minerals. *Earth Planet. Sci. Lett.* **374**, 156–163.

Associate editor: Pierre Beck